

# Thermally boosted upconversion and downshifting luminescence in $\text{Sc}_2(\text{MoO}_4)_3:\text{Yb}/\text{Er}$ with two-dimensional negative thermal expansion

Jinsheng Liao (✉ [jsliao1209@126.com](mailto:jsliao1209@126.com))

Jiangxi University of Science and technology

Minghua Wang

Jiangxi University of Science and technology

Fulin Lin

Fujian Institute of Research on the Structure of Matter, Chinese Academy of Sciences

Zhuo Han

Jiangxi University of Science and technology

Datao Tu

Fujian Institute of Research on the Structure of Matter, Chinese Academy of Sciences

Xueyuan Chen

Fujian Institute of Research on the Structure of Matter, Chinese Academy of Sciences

<https://orcid.org/0000-0003-0493-839X>

Bao Qiu

Ningbo Institute of Materials Technology & Engineering <https://orcid.org/0000-0002-7505-6135>

Herui Wen

Jiangxi University of Science and Technology

---

## Article

**Keywords:** photoluminescence, negative thermal expansion, lanthanide-doped phosphors

**Posted Date:** October 13th, 2021

**DOI:** <https://doi.org/10.21203/rs.3.rs-952130/v1>

**License:**   This work is licensed under a Creative Commons Attribution 4.0 International License.

[Read Full License](#)

---

**Version of Record:** A version of this preprint was published at Nature Communications on April 19th, 2022. See the published version at <https://doi.org/10.1038/s41467-022-29784-6>.

# Thermally boosted upconversion and downshifting luminescence in

## $\text{Sc}_2(\text{MoO}_4)_3:\text{Yb}/\text{Er}$ with two-dimensional negative thermal expansion

Jinsheng Liao<sup>1\*</sup>, Minghua Wang<sup>1</sup>, Fulin Lin<sup>2</sup>, Zhuo Han<sup>1</sup>, Datao Tu<sup>2\*</sup>, Xueyuan Chen<sup>2\*</sup>, Bao Qiu<sup>3\*</sup>, He-Rui Wen<sup>1</sup>

<sup>1</sup>*School of Chemistry and Chemical Engineering, Jiangxi University of Science and Technology, Ganzhou 341000, China*

<sup>2</sup>*CAS Key Laboratory of Design and Assembly of Functional Nanostructures, and Fujian Key Laboratory of Nanomaterials, Fujian Institute of Research on the Structure of Matter, Chinese Academy of Sciences, Fuzhou, Fujian 350002, China*

<sup>3</sup>*Ningbo Institute of Materials Technology & Engineering (NIMTE), Chinese Academy of Sciences, Ningbo, Zhejiang, 315201, P. R. China*

\* Corresponding author

E-mail address: [jsliao1209@126.com](mailto:jsliao1209@126.com), [dttu@fjirsm.ac.cn](mailto:dttu@fjirsm.ac.cn), [xchen@fjirsm.ac.cn](mailto:xchen@fjirsm.ac.cn), [qiubao@nimte.ac.cn](mailto:qiubao@nimte.ac.cn)

Lanthanide ( $\text{Ln}^{3+}$ )-doped phosphors generally suffer from thermal quenching, in which their photoluminescence (PL) intensities decrease at the higher temperature. Herein, we report a class of unique two-dimensional negative-thermal-expansion phosphor of  $\text{Sc}_2(\text{MoO}_4)_3:\text{Yb}/\text{Er}$ . By virtue of the reduced distances between sensitizers and emitters as well as confined energy migration with increasing the temperature, a 45-fold enhancement of green upconversion (UC) luminescence and a 450-fold enhancement of near-infrared downshifting (DS) luminescence of  $\text{Er}^{3+}$  are achieved from 25 to 500 °C. The thermally boosted UC and DS luminescence mechanism is systematically investigated through *in situ* temperature-dependent Raman spectroscopy, synchrotron X-ray diffraction and PL dynamics. Moreover, the luminescence lifetime of  $^4\text{I}_{11/2}$  of  $\text{Er}^{3+}$  in  $\text{Sc}_2(\text{MoO}_4)_3:\text{Yb}/\text{Er}$  displays a strong temperature dependence, enabling ratiometric thermometry with the highest relative sensitivity of 13.4%/K at 298 K. These findings may gain a vital insight into the design of negative-thermal-expansion  $\text{Ln}^{3+}$ -doped phosphors for versatile applications.

The photoluminescence (PL) intensity of lanthanide ( $\text{Ln}^{3+}$ )-doped phosphors is usually quenched with increasing temperature, which is referred to as positive thermal quenching<sup>1-4</sup>. This phenomenon has been frequently observed in most phosphors due to the vibration aggravation with temperature to promote the domination of non-radiative multiphonon transition probability (Fig. 1a). Such a phenomenon greatly limits the application of luminescent materials in the high-temperature region, which causes degeneration of device performance and eventually system failure. If no obvious decrease of PL intensity occurs on heating, the phosphor would show zero-thermal-quenching performance<sup>5,6</sup>. This pathway can occur in the compensation of emission loss through the polymorphism modification of the host, wherein the energy transfer (ET) from electron-hole pairs to the excited state energy levels results in radiative recombination in close proximity at the thermally activated defect levels (Fig. 1b).

Hitherto, several phosphors have been reported to exhibit abnormal thermo-enhanced luminescence during heating<sup>7-10</sup>. Most of such abnormal thermally enhanced UC luminescence is observed in  $\text{Ln}^{3+}$ -doped inorganic materials with three-dimensional negative-thermal expansion characteristics (NTE)<sup>9,10</sup>, where all the three cell parameters of the doped crystals shrink at elevated temperature. The host lattice shrinkage at high temperature may induce the decrease of distance between the sensitized ions and the activated ions to improve the ET efficiency, resulting in the enhancement of luminescence intensity<sup>9-11</sup>. At present, only a few NTE host materials are demonstrated to be suitable for  $\text{Ln}^{3+}$  doping and their luminescence performance is usually too poor to fulfill their practical applications. As such, more and more works have been devoted to the exploration of novel inorganic materials with NTE properties (Fig. 1c)<sup>12-17</sup>.

In this work, we report the synthesis and characterization of a phosphor based on  $\text{Yb}^{3+}/\text{Er}^{3+}$  co-doped NTE matrix of  $\text{Sc}_2(\text{MoO}_4)_3$  with a unique two-dimensional NET coefficient ( $\alpha_a=-8.62\times 10^{-6}/\text{K}$ ,  $\alpha_b=4.25\times 10^{-6}/\text{K}$ ,  $\alpha_c=-6.35\times 10^{-6}/\text{K}$ ) (Fig. 1d). The distance of  $\text{Ln}^{3+}$  dopants in the matrix can be manipulated with temperature to realize the thermal enhanced both UC and DS emission of  $\text{Er}^{3+}$  upon 980-nm excitation. We ap-

ply *in situ* temperature-dependent Raman spectroscopy, synchrotron X-ray diffraction and luminescence dynamics to reveal the mechanism of negative-thermal effects. It is demonstrated that the thermally boosted UC and DS emissions can be achieved benefitting from the lattice shrinkage and confined energy migration at elevated temperatures. Moreover, the NIR-II PL lifetime of  $\text{Er}^{3+}$  in  $\text{Sc}_2(\text{MoO}_4)_3:\text{Yb}/\text{Er}$  (SMO:Yb/Er) phosphors is found to be increased by more than two orders of magnitude as the temperature increasing from 25 to 425 °C. As such, we employ the proposed phosphors for luminescent lifetime-based temperature sensing.

## Results

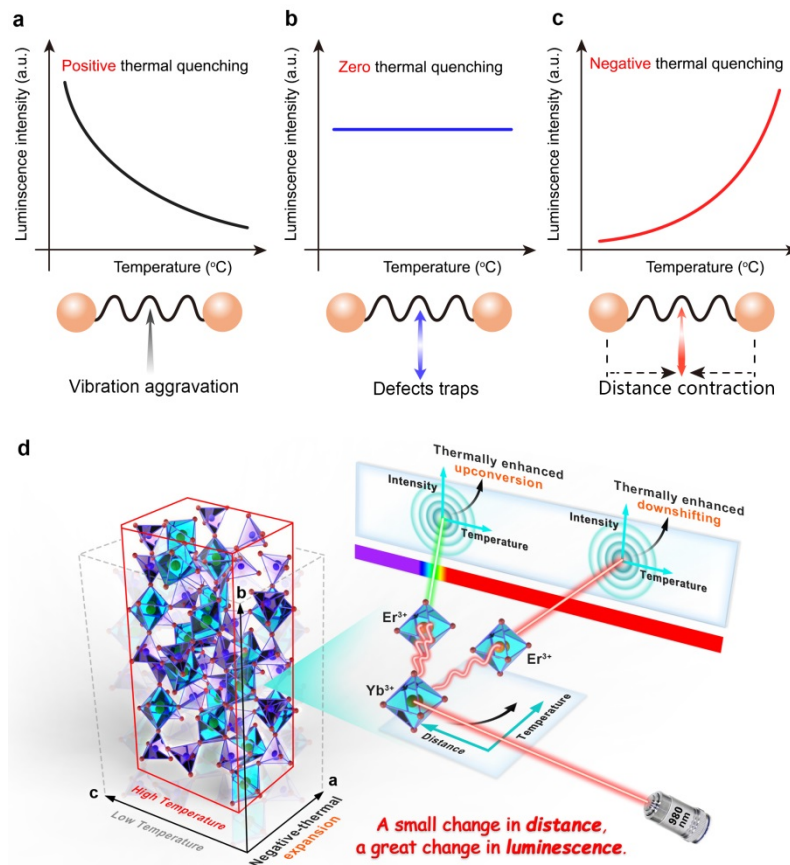


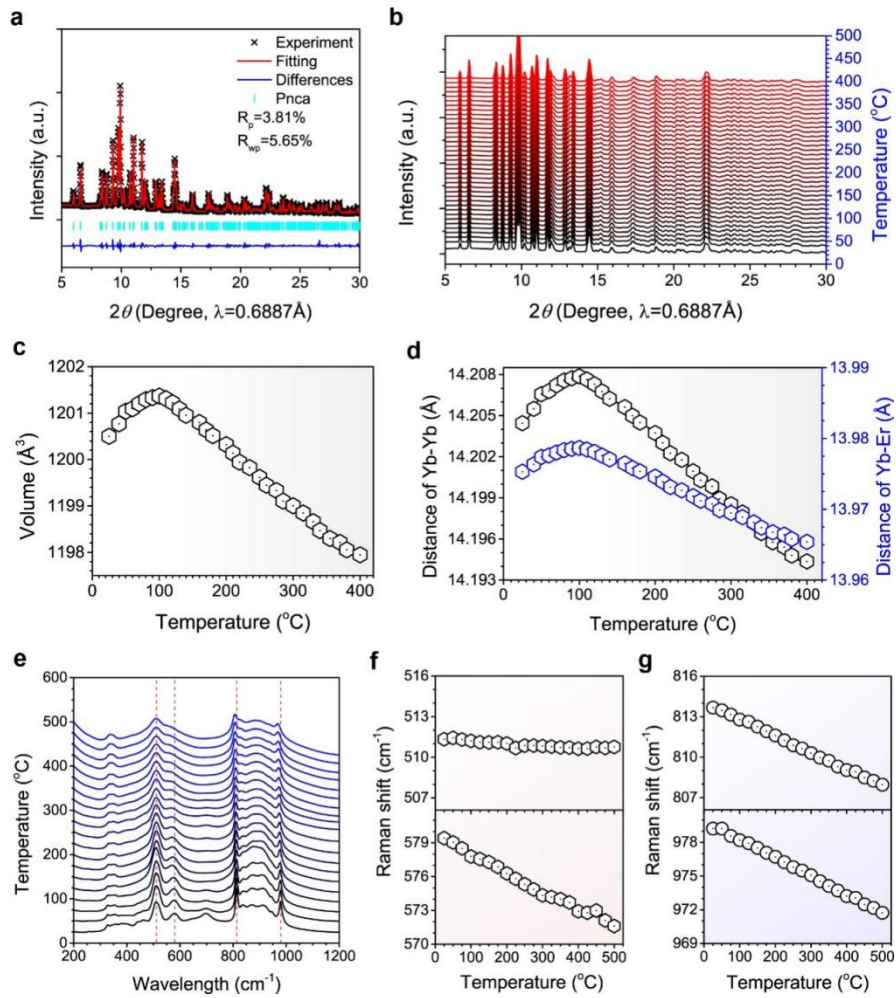
**Figure 1| Scheme of thermal-dependence effects in phosphor.** **a.** Positive thermal quenching phenomenon. Temperature raising may aggravate the vibration of atoms to promote the domination of nonradiative multiphonon transition probability. **b.** Zero thermal quenching phenomenon. Temperature raising excites the electron-hole pairs at the defect traps to the excited state energy levels to enhance the radiative recombination. **c.** Negative-thermal quenching (thermal-enhanced) phenomenon. Temperature raising causes distance contraction, resulting in higher energy transfer efficiency and lattice distortion to improve the radiative transition probability. **d.** Schematic illustration of the negative-thermal-index in  $\text{Sc}_2(\text{MoO}_4)_3:\text{Yb}/\text{Er}$ , indicating that both the a-axis and c-axis contract while the b-axis expands at high temperature.

## Negative-thermal expansion in $\text{Sc}_2(\text{MoO}_4)_3\text{:Yb/Er}$

SMO:Yb/Er phosphors were synthesized via a sol-gel method. The basic structures of the SMO:Yb/Er samples with different dopant concentrations were detected by X-ray diffraction (XRD) patterns (Supplementary Fig. 1). All the structures of the as-prepared samples are well consistent with the orthorhombic  $\text{Sc}_2(\text{MoO}_4)_3$  (ICSD#20838) without any observable impurities. Their chemical compositions and morphologies were determined by energy dispersive X-ray spectroscopy (EDX) and scanning electron microscopy (SEM), respectively (Supplementary Fig. 2). It can be observed that the as-prepared SMO:Yb/Er samples are microcrystals with sizes of 1–2  $\mu\text{m}$  and Sc, Yb, Er, Mo and O elements are homogeneously distributed in the matrix.

Fig. 2a shows the *Rietveld* refinement of the synchrotron XRD (SXR) patterns measured at room temperature for the SMO:Yb/Er phosphors. All the diffraction peaks can be well indexed by orthorhombic cell (space group: *Pnab*). *In situ* temperature-dependent SXR was applied to reveal their thermal expansion behavior from 25 to 400  $^{\circ}\text{C}$ . The diffraction peaks on the whole temperature range are well in accordance with the orthorhombic SMO crystal, which suggests that no obvious phase change happened with increasing of the temperature. Based on these SXR patterns, lattice constants as a function of temperature are calculated (Supplementary Fig. 3). With the increase of temperature, the a-axis contracts, and the b-axis expands steadily, while the c-axis first expands and then contracts. The axial expansion coefficients were determined to be  $\alpha_a = -8.62 \times 10^{-6}/\text{K}$ ,  $\alpha_b = 4.25 \times 10^{-6}/\text{K}$ ,  $\alpha_c = -6.35 \times 10^{-6}/\text{K}$ . Note that almost all the reported  $\text{Ln}^{3+}$ -doped NET phosphors show three-dimensional negative thermal expansion while SMO:Yb/Er phosphors exhibit only two-dimensional negative thermal expansion. As such, the energy migration between  $\text{Ln}^{3+}$  dopants may be effectively confined within the two-dimensional layered structures for producing intense PL emissions with increasing the temperature<sup>18</sup>.

Pure orthorhombic SMO crystal is composed of corner-sharing  $\text{ScO}_6$  octahedra and  $\text{MoO}_4$  tetrahedra. Sc and Mo are located in the center of octahedron and tetrahedron, respectively, which would reciprocally rotate at elevated temperature to



result in the lattice shrinkage. The calculated cell volume variation is similar to that of the lattice parameter  $c$  as shown in Fig. 2c. Such thermal expansion behavior has been also observed for pure SMO<sup>19-21</sup>. Nevertheless, the volume contraction coefficient ( $\alpha_v = -10.70 \times 10^{-6}/\text{K}$ ) of SMO:Yb/Er is more negative than that of pure SMO ( $\alpha_v = -6.30 \times 10^{-6}/\text{K}$ )<sup>6</sup>, due to the substitution of  $\text{Sc}^{3+}$  by  $\text{Ln}^{3+}$  dopants (*i.e.*,  $\text{Yb}^{3+}$  and  $\text{Er}^{3+}$ ) with larger radius.

For the case of homogeneous doping of Ln<sup>3+</sup> ions in SMO, the average distance ( $R_T$ ) between the Yb<sup>3+</sup> and Er<sup>3+</sup> ions for different temperatures can be estimated by the following formula<sup>22</sup>:

$$R_T = 2 \left( \frac{3V_T}{4\pi NX_c} \right)^{\frac{1}{3}} \quad (1)$$

where  $V_T$  is the volume of the unit cell for different temperatures (Fig. 2c),  $X_c$  is the doping concentration, and  $N$  is the number of available crystallographic sites occupied by the activator ions in unit cell ( $N=4$ ). The distances of the Yb<sup>3+</sup>-Yb<sup>3+</sup> ions and Yb<sup>3+</sup>-Er<sup>3+</sup> ions in SMO:Yb/Er phosphors with different temperatures were calculated by the above formula (Fig. 2d). The result indicates that the distances of Yb<sup>3+</sup>-Er<sup>3+</sup> ions (13.975 Å, at 25 °C) decreased at higher temperature, which may benefit the improvement of the ET efficiency between Yb<sup>3+</sup>-Er<sup>3+</sup><sup>23</sup>. In addition, the longer distance of two adjacent Er<sup>3+</sup> ions at higher temperature (38.529 Å, at 400 °C) may also reduce the cross-relaxation ( ${}^4F_{7/2}+{}^4I_{11/2} \rightarrow {}^4F_{9/2}+{}^4F_{9/2}$ ) to suppress the red emission ( ${}^4F_{9/2} \rightarrow {}^4I_{15/2}$ ) of Er<sup>3+</sup><sup>24</sup>.

Raman spectroscopy is a valuable tool to evaluate the change of local structure<sup>25, 26</sup>. *In situ* temperature-dependent Raman spectra are shown in Fig. 2e. The observed mode with a frequency of 341 cm<sup>-1</sup> corresponds to the bending mode of MoO<sub>4</sub> tetrahedra. When the temperature increases, this Raman peak exhibits a blue shift (Fig. 2f). The median frequency B<sub>1g</sub> mode of SMO is observed at 511 cm<sup>-1</sup>. The higher frequency A<sub>g</sub> at 979 cm<sup>-1</sup> (the maximum phonon energy) is related to symmetric stretching modes of the MoO<sub>4</sub> tetrahedra (Fig. 2g), and the modes with frequencies in the range of 814-855 cm<sup>-1</sup> are attributed to asymmetric stretching modes of the MoO<sub>4</sub> tetrahedra<sup>27</sup>. As the temperature increases from 25 to 500 °C, the Raman peak of 979 cm<sup>-1</sup> redshifts to 971 cm<sup>-1</sup>, which implies an extensive deformation in the crystal through translational and/or rotational motions of the MoO<sub>4</sub> tetrahedral units<sup>28</sup>. The reduction of maximum phonon energy may benefit the luminescence of Ln<sup>3+</sup> at elevated temperatures.

### **Thermally enhanced upconversion emission**

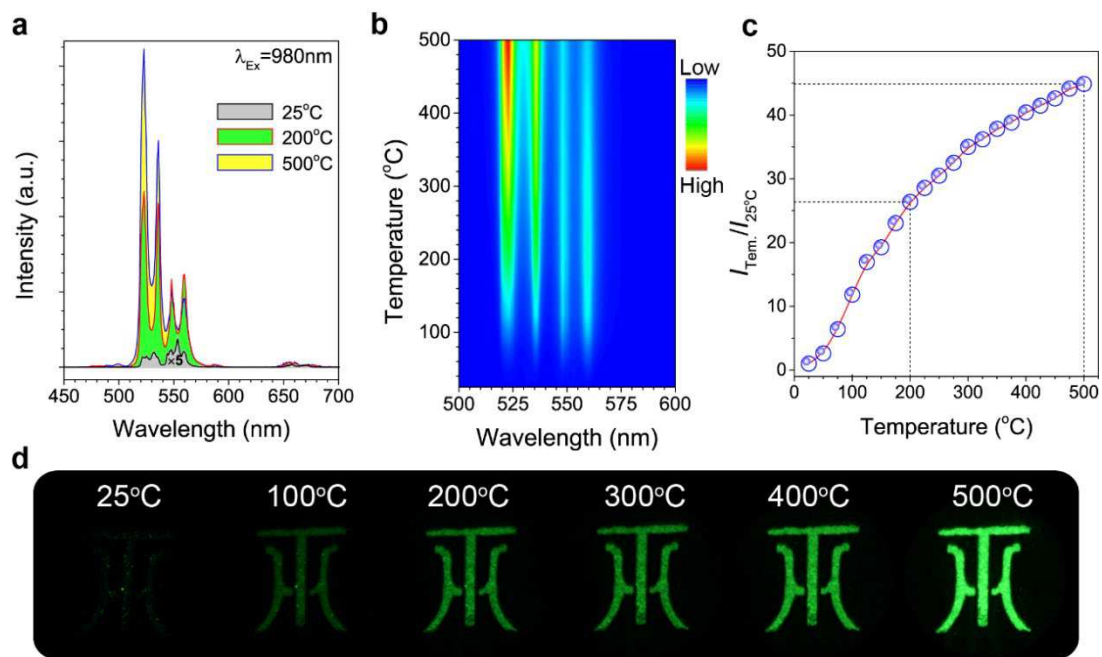


**Figure 3 | Thermally enhanced upconversion emission.** a. UC spectra of SMO:Yb/Er phosphor with different temperatures. b. Two-dimensional UC emission topographical mapping within the temperature from 25 to 500 °C. c. Normalized UC emission intensity as a function of temperature. d. UC photographs of SMO:Yb/Er phosphors at various temperatures by the Nikon D750 camera upon 980 nm excitation.

Figs. 3a and 3b show the UC emission spectra of the SMO:Yb/Er phosphors upon 980-nm laser excitation at different temperatures. Two intense green emission bands peaking at 522 and 558 nm are observed, which correspond to the  $^2\text{H}_{11/2} \rightarrow ^4\text{I}_{15/2}$  and  $^4\text{S}_{3/2} \rightarrow ^4\text{I}_{15/2}$  transitions of  $\text{Er}^{3+}$ , respectively. A weak red emission band peaking at 654 nm of  $\text{Er}^{3+}$  is attributed to the  $^4\text{F}_{9/2} \rightarrow ^4\text{I}_{15/2}$  transition<sup>18</sup>. In Fig. 3c, two temperature regions for the UC emissions can be observed. When temperature increases from 25 to 200 °C, the overall green emission intensity increases by 26 fold. When the temperature increased from 200 to 500 °C, the UC intensity can be further increased. Specifically, the overall UCL intensity increases by 45 fold from 25 to 500 °C. To explicitly show the changes of brightness, we provide the photographs of logo for Jiangxi University of Science and Technology (JXUST) made by SMO:Yb/Er phosphors with increasing temperatures (Fig. 3d). Upon 980-nm laser diode excitation, it can be seen that the logo becomes brighter with the increase in temperature.

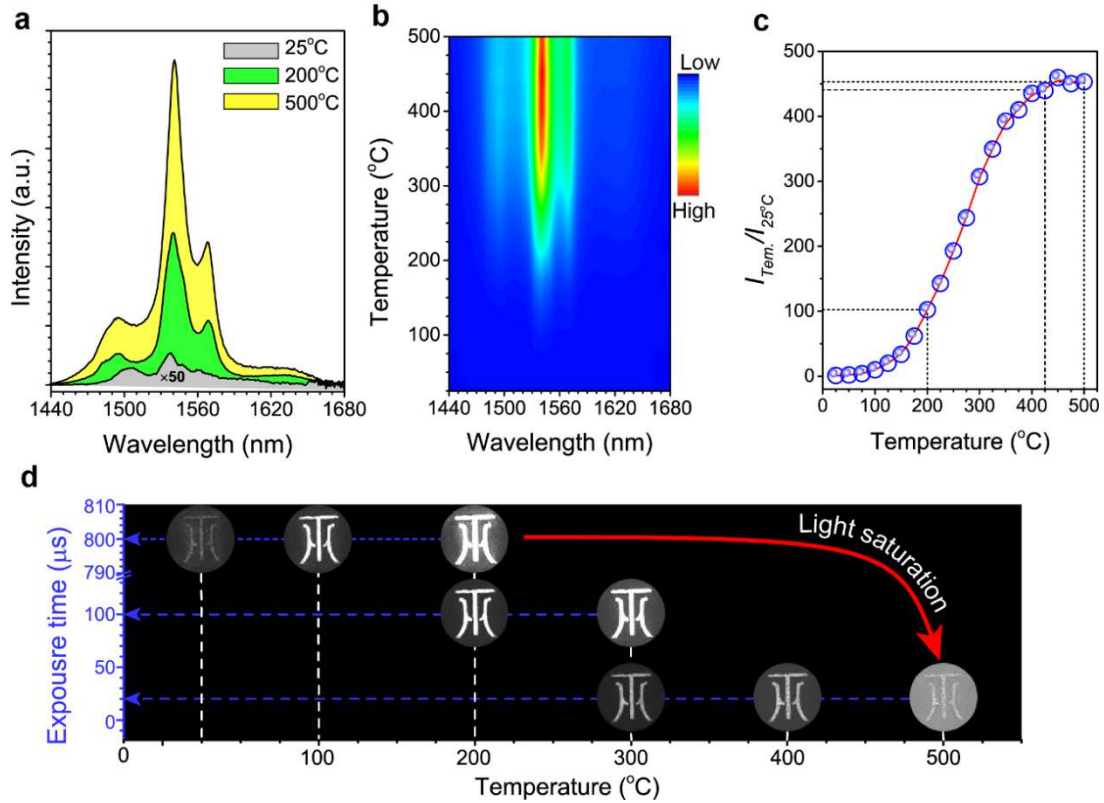


**Figure 4 | Thermally enhanced downshifting emission.** **a.** DS emission spectra of SMO:Yb/Er phosphor with different temperatures. **b.** Two-dimensional DS emission topographical mapping with the temperature from 25 to 500 °C. **c.** Normalized DS emission intensity as a function of temperature. **d.** Photographs of SMO:Yb/Er at various temperatures by a NIR camera. To avoid interference of 980 nm laser, the 1250 nm filter has been added in the front of Photonic Science InGaAs camera.

Fig. 4a shows the temperature-dependent DS emission spectra of the SMO:Yb/Er phosphors upon excitation at 980 nm. The spectra exhibit characteristic near-infrared II (NIR-II) emission of  $\text{Er}^{3+}$  peaking at 1538 nm, which originates from the  $^4I_{13/2} \rightarrow ^4I_{15/2}$  transition. The emission intensity also displays a significant enhancement with increasing the temperature from 25 to 500 °C (Fig. 4b), where a 450-fold enhancement of the integrated luminescence intensity was achieved (Fig. 4c). Fig. 4d shows the temperature-dependent NIR photographs of logo for JXUST made by SMO:Yb/Er phosphors. Upon 980-nm laser excitation, the logo of JXUST also became brighter by a NIR camera with the increase of temperature. Due to the low pixel size of current near-infrared cameras, the shortened exposure time may reduce light saturation. As the temperature increases, the DS luminescence sharply increas-

es. Therefore, we chose different exposure times in different temperature regions to take the photographs.

### **Thermally enhanced photoluminescence mechanism**

To shed more light on the mechanism responsible for the thermal-enhanced UC and DS emissions, the temperature-dependent luminescence of  $\text{Yb}^{3+}$  was investigated. Fig. 5a displays the excited state ( $^2\text{F}_{5/2}$ ) lifetime of  $\text{Yb}^{3+}$  in  $\text{SMO}:\text{Yb}/\text{Er}$ . It exhibits a marked increase in the PL lifetime from 16.62 to 278  $\mu\text{s}$  as the temperature was raised from 25 to 200  $^{\circ}\text{C}$ . Generally, the radiation trapping of  $\text{Yb}^{3+}$  may lengthen the PL lifetimes in phosphors<sup>29,30</sup>, because the lattice contraction may shorten the distance of  $\text{Yb}^{3+}\text{-Yb}^{3+}$  at elevated temperature to promote the radiation trapping of  $\text{Yb}^{3+}$  (Supplementary Fig. 3). In  $\text{Yb}^{3+}\text{-Er}^{3+}$  codoped phosphors,  $\text{Yb}^{3+}$  acts as not only radiation-trapping to store energy but also as a sensitizer to transfer the energy to  $\text{Er}^{3+}$ . These radiation trappings may enhance the emission of  $\text{Er}^{3+}$ . Moreover, the distance of  $\text{Yb}^{3+}\text{-Er}^{3+}$  becomes shorter with an increase of the temperature. The ET processes between sensitizer ( $\text{Yb}^{3+}$ ) to activator ( $\text{Er}^{3+}$ ) are usually considered to occur through dipolar-dipolar interactions, whose ET efficiency is proportional to  $r^{-6}$  ( $r$  is the average donor-acceptor distance)<sup>31</sup>. As such, the ET efficiency can be greatly improved at elevated temperature. Correspondingly, both the UC and DS emissions of  $\text{SMO}:\text{Yb}/\text{Er}$  were significantly enhanced when the temperature increased.

Moreover,  $\text{Yb}_2\text{WO}_6:1\%\text{Er}$  with normal positive-thermal expansion was adopted as a comparative investigation<sup>9</sup>. As expected, thermally quenched PL emission was detected when the temperature increased from 25 to 300  $^{\circ}\text{C}$  (see Supplementary Figs. 4 and 5), since the increased distance between  $\text{Yb}^{3+}$  to  $\text{Er}^{3+}$  would reduce the ET efficiency from  $\text{Yb}^{3+}$  to  $\text{Er}^{3+}$ . To reveal the role of the sensitizer of  $\text{Yb}^{3+}$ ,  $\text{Er}^{3+}$  single-doped SMO and  $\text{Yb}^{3+}$  single-doped SMO phosphors were also synthesized. From the temperature-dependent PL emission spectra of the  $\text{SMO}:\text{Er}$  (5%) phosphors (Supplementary Fig. 6), the UC emission intensity of  $\text{Er}^{3+}$  decreases with the increase of temperature upon 980-nm excitation without the ET from  $\text{Yb}^{3+}$  to  $\text{Er}^{3+}$  due to the detrimental cross-relaxation process between  $\text{Er}^{3+}$  ions. Meanwhile, the NIR-II DS emission of  $\text{Er}^{3+}$

for SMO:Er (5%) phosphors improved by only 5.9-fold with the increase of temperature (Supplementary Fig. 7), which is greatly less than the enhanced factor of SMO:Yb/Er phosphors. These results verify that the contribution of ET from the sensitizer (Yb<sup>3+</sup>) to the activator (Er<sup>3+</sup>) is essential for achieving efficient UC and DS luminescence of Er<sup>3+</sup>.

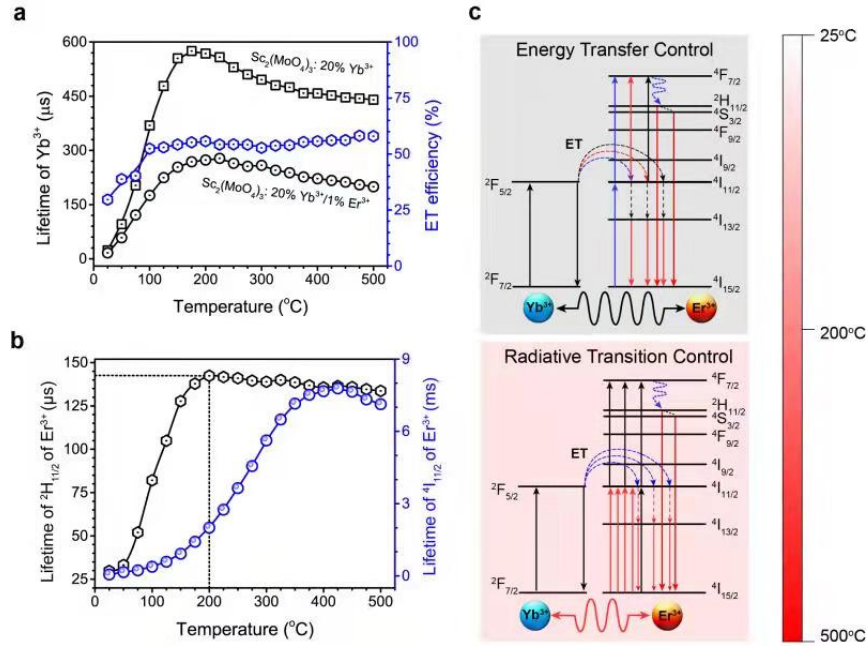


**Figure 5 | Thermally enhanced photoluminescence mechanism** **a.** Temperature-dependent luminescence lifetime of  $^2F_{5/2}$  excited state of Yb<sup>3+</sup> in Yb<sup>3+</sup>/Er<sup>3+</sup>-codoped and Yb<sup>3+</sup>-single doped SMO, respectively. Temperature-dependent energy transfer efficiency of Yb<sup>3+</sup>-to-Er<sup>3+</sup>. **b.** Temperature-dependent lifetimes of  $^2H_{11/2}$  (522 nm) and  $^4I_{11/2}$  (1538 nm) excited states of Er<sup>3+</sup> in SMO:Yb/Er, respectively. **c.** Energy level diagram of green UC (NIR DS) emission showing the proposed temperature dependence of electronic transition and energy-transfer processes in SMO:Yb/Er.

For Yb<sup>3+</sup>-doped SMO phosphors, the excited state ( $^2F_{5/2}$ ) lifetime of Yb<sup>3+</sup> exhibits a similar change trend as that of SMO:Yb/Er (Fig. 5a). Without the ET from Yb<sup>3+</sup> to Er<sup>3+</sup>, the excited state ( $^2F_{5/2}$ ) lifetime of Yb<sup>3+</sup> for SMO:Yb phosphors was determined to be longer than that of SMO:Yb/Er at the same temperature. The ET efficiency ( $\eta_{ET}$ ) can be calculated from the following expression<sup>32</sup>:

$$\eta_{ET} = 1 - \frac{\tau_{Yb-Er}}{\tau_{Yb}} \quad (2)$$

where  $\tau_{\text{Yb-Er}}$  and  $\tau_{\text{Yb}}$  are the PL lifetimes of  $\text{Yb}^{3+}$  at 1051 nm in SMO:Yb/Er and SMO:Yb phosphors (see the luminescence decay curves of Supplementary Fig. 8), respectively. Accordingly, it was determined that the ET efficiency from  $\text{Yb}^{3+}$  to  $\text{Er}^{3+}$  in SMO:Yb/Er increased gradually when the temperature was raised from 25 to 200 °C (Fig. 5a). For the temperature above 200 °C, the ET efficiency kept almost constant (~55%). However, the overall UC and DS emission intensities of SMO:Yb/Er crystal continued to increase in this temperature region.

To figure out this contradiction, the temperature-dependent UC PL lifetime of  ${}^2\text{H}_{11/2}$  for  $\text{Er}^{3+}$  was measured ( Fig. 5b). It exhibited a dramatic increase from 29.77 to 141.67  $\mu\text{s}$  with the temperature rise from 25 to 200 °C, which implies that the non-radiative transition of  ${}^2\text{H}_{11/2} \rightarrow {}^4\text{I}_{15/2}$  was inhibited at elevated temperature. Nevertheless, only a tiny change was observed for the PL lifetime of  ${}^2\text{H}_{11/2}$  for  $\text{Er}^{3+}$  with the temperature above 200 °C. Note that a similar trend was also observed for the PL lifetime of  $\text{Yb}^{3+}$  in SMO:Yb. The luminescence lifetime ( $\tau$ ) of an excited state is determined by  $\tau = 1/(A_r + A_{nr})^{33,34}$ , where  $A_r$  and  $A_{nr}$  are the radiative and nonradiative transition probabilities of this energy level, respectively. Accordingly, it is deduced that the increase of  $A_r$  is nearly equal to the decrease of  $A_{nr}$ . The promoted  $A_r$  and inhibited  $A_{nr}$  in the  $\text{Ln}^{3+}$  dopant indicate that lattice distortion enhances a crystal field with odd parity and modifies local symmetry of activator ions via the NTE effect. Based on the above analysis, the thermally enhanced UC emission with the temperature from 25 to 200 °C is mainly governed by the ET from  $\text{Yb}^{3+}$  to  $\text{Er}^{3+}$ . For the temperature above 200 °C, the thermally enhanced UC emission is mainly controlled by the radiation transition of  $\text{Er}^{3+}$  that is strengthened with an increase of temperature (Fig. 5c).

To reveal the mechanism responsible for the negative-thermal DS luminescence of SMO:Yb/Er, we measured the temperature-dependent PL decays of  ${}^4\text{I}_{11/2}$  of  $\text{Er}^{3+}$ , which can be well fitted by a single-exponential function (Supplementary Fig. 9). When the temperature increased from 25 to 200 °C, it was determined that the PL lifetime of  ${}^4\text{I}_{11/2}$  level of  $\text{Er}^{3+}$  increased markedly from 61.2  $\mu\text{s}$  to 2004  $\mu\text{s}$ . Meanwhile, the  $\text{Yb}^{3+}$ - $\text{Er}^{3+}$  ET efficiency of the SMO:Yb/Er crystal increased from 29% to 55% with

increasing the temperature (see Fig. 5a). According to the previous analysis of UC process, the thermally enhanced DS luminescence for this temperature region was mainly governed by the energy transfer from Yb<sup>3+</sup> to Er<sup>3+</sup>. Besides, the PL lifetime of <sup>4</sup>I<sub>11/2</sub> level of Er<sup>3+</sup> increased from 2004 to 7789 μs as the temperature rise from 200 to 425 °C. At higher temperature above 425 °C, the PL lifetime of <sup>4</sup>I<sub>11/2</sub> level of Er<sup>3+</sup> decreased, which indicated that the increase of A<sub>r</sub> was larger than the decrease of A<sub>nr</sub>. These results demonstrate that NIR DS emission with the temperature from 200 to 425 °C was also enhanced via the control of radiative transition (Fig. 5c).

### Photoluminescence lifetime-based thermal sensing

The tunable PL lifetime of Er<sup>3+</sup> in SMO:Yb/Er phosphors, which spans two orders of magnitude with the temperature from 25 to 425 °C, offering a great opportunity for their application in lifetime-based luminescent thermometry (LLT). Note that LLT is of special importance owing to several attractive merits over conventional intensity-based thermometry<sup>35-37</sup>. For instance, PL lifetime is insensitivity to the variation in phosphors concentration and excitation intensity, which enables LLT to circumvent the measurement error that is intrinsic and inevitable for intensity-based thermometry. In addition, for the conventional intensity-based thermometry, the intensity signal may become unreliable at different depths since the signal-to-noise ratio may be very low when the depth-induced quenching of the intensity signal is serious. By contrast, the lifetime signal remains essentially unaltered at different depths.

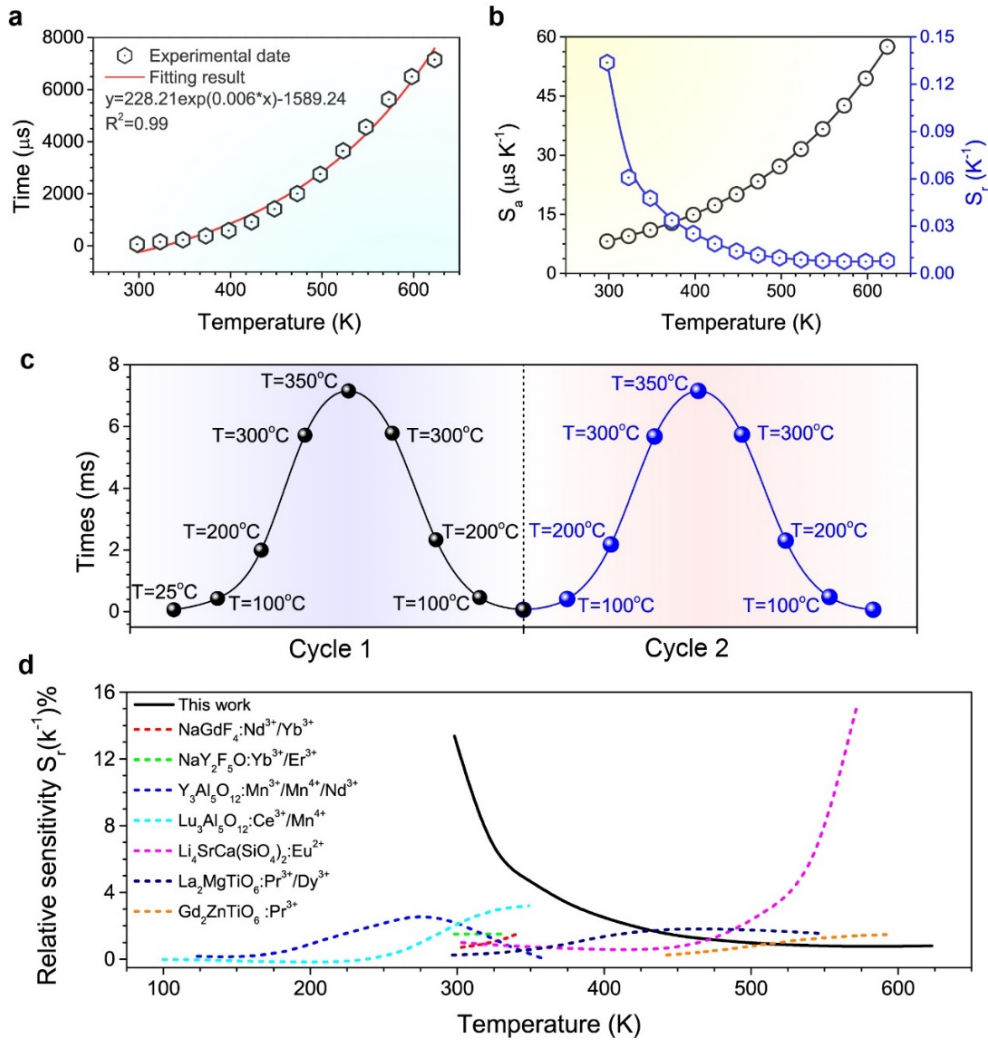
For SMO:Yb/Er phosphors, the plot of calculated lifetime value (τ, μs) and temperature (T, K) is presented in Fig. 6a, where the dependence of lifetime on temperature can be well fitted by the following equation:

$$\tau(T) = -1589.24 + 228.21 \exp(0.006T) \quad (3)$$

Furthermore, the absolute temperature sensitivity (S<sub>a</sub>) and relative temperature sensitivity (S<sub>r</sub>) based on the luminescence lifetime of Er<sup>3+</sup> are calculated according to the following equations (Fig. 6b), respectively<sup>38</sup>:

$$S_a = \left| \frac{d\tau}{dT} \right| \quad (4)$$

$$S_r = \left| \frac{1}{\tau} \cdot \frac{d\tau}{dT} \right| \quad (5)$$



The optimal  $S_a$  and  $S_r$  were determined to be as high as  $57.51 \mu\text{s K}^{-1}$  and  $13.4\% \text{ K}^{-1}$ , respectively. Temperature-recycle measurements demonstrated that the SMO:Yb/Er can provide excellent thermal sensing repeatability (Fig. 6c). For comparison, we also displayed other state-of-the-art luminescent thermometry materials (Fig. 6d). The optimal  $S_r$  value of SMO:Yb/Er was observed to be an order of magnitude higher than that of other majority LLTs<sup>39,40-44</sup>.

To compare the  $S_r$  with the traditional intensity-based thermometry, we list the representative optical ratiometric thermometry methods with emission bands lying within the NIR window (Table S1). The LLT of SMO:Yb/Er phosphor also exhibits a very high  $S_r$  value. Specifically, the optimal  $S_r$  value of SMO:Yb/Er is observed to be ten times higher than that of LuVO<sub>4</sub>:Yb/Er@SiO<sub>2</sub><sup>45</sup> and more than twice higher relative to that of LaF<sub>3</sub>:Yb/Er@LaF<sub>3</sub>:Yb/Tm<sup>46</sup>. All these results indicate that SMO:Yb/Er phosphor can be explored as an ideal candidate for LLT-based temperature sensing with high  $S_r$ .

## Discussion

In summary, a novel two-dimensional negative-thermal phosphor of SMO:Yb/Er has been proposed. The negative-thermal effect was systematically investigated by *In situ* temperature-dependent Raman spectroscopy, synchrotron X-ray diffraction and luminescence dynamics. We achieved 45-fold and 450-fold thermally enhanced UC luminescence and NIR-II DS emission of Er<sup>3+</sup> from 25 to 500 °C, which originated from the thermally promoted energy transfer with increasing temperature. By virtue of the tunable PL lifetime of Er<sup>3+</sup> at different temperatures, the proposed phosphors were employed for LLT-based temperature sensing, which can circumvent the intrinsic limitations of poor temperature sensitivity based on the conventional intensity-based thermometry. These findings open up a new avenue for the exploration of thermal-enhanced quenching phosphors with excellent UC and DS luminescence for versatile applications.

## Experimental section

**Synthesis of Sc<sub>2</sub>(MoO<sub>4</sub>)<sub>3</sub>:Yb/Er.** A series of different Yb<sup>3+</sup> (Er<sup>3+</sup>) doping concentrations of Sc<sub>2</sub>(MoO<sub>4</sub>)<sub>3</sub>:Yb/Er phosphors were synthesized by a sol-gel method<sup>47</sup>. All the chemicals of Sc<sub>2</sub>O<sub>3</sub> (99.99%, Ganzhou Guangli High-tech Materials Co. Ltd), Yb<sub>2</sub>O<sub>3</sub> (99.99%, Ganzhou Guangli High-tech Materials Co. Ltd), Er<sub>2</sub>O<sub>3</sub> (99.99%, Ganzhou Guangli High-tech Materials Co. Ltd), (NH<sub>4</sub>)<sub>6</sub>Mo<sub>7</sub>O<sub>24</sub>·4H<sub>2</sub>O (AR, Shanghai Aladdin Biochemical Tech-

nology Co., Ltd.),  $\text{HNO}_3$ ,  $\text{C}_2\text{H}_5\text{NO}_2$ ,  $\text{C}_6\text{H}_8\text{O}_7 \cdot \text{H}_2\text{O}$  were used as raw materials. Firstly, the nitrates of all the rare-earth oxides were obtained by dissolution in dilute nitric acid.  $(\text{NH}_4)_6\text{Mo}_7\text{O}_{24} \cdot 4\text{H}_2\text{O}$  (Shanghai Aladdin Biochemical Technology Co., Ltd.) and  $\text{C}_2\text{H}_5\text{NO}_2$  were dissolved in a suitable volume of de-ionized water, respectively. The solution of  $(\text{NH}_4)_6\text{Mo}_7\text{O}_{24} \cdot 4\text{H}_2\text{O}$  and  $\text{C}_2\text{H}_5\text{NO}_2$  was slowly dropped into the solution containing rare-earth nitrates, into which a certain of citric acid as a chelating agent (citric acid/metal ion=2:1) was added. The above solution was heated at  $80\text{ }^\circ\text{C}$  to produce a light yellow transparent gel, which was further dried at  $120\text{ }^\circ\text{C}$  for 24 h to get the yellow dried gel. Finally, the dried gel was annealed at  $800\text{ }^\circ\text{C}$  for 3 h in air. The white powder samples obtained via natural cooling were used for further characterization. A series of  $\text{Sc}_{2(1-x-y)}(\text{MoO}_4)_3 \cdot x\text{Yb}/y\text{Er}$  ( $x=0, 1\%, 5\%, 10\%, 15\%, 20\%, 25\%$ ;  $y=0, 0.1\%, 0.5\%, 1\%, 2\%, 4\%, 8\%$ ) powders were prepared.

**Synthesis of  $\text{Er}^{3+}$ -doped  $\text{Yb}_2\text{WO}_6$ .** According to the stoichiometric composition of  $\text{Yb}_{1.98}\text{Er}_{0.02}\text{WO}_6$ , all the reactants were weighed and mixed thoroughly in an agate mortar, then sintered in a tubular furnace at  $1300\text{ }^\circ\text{C}$  for 4h in air. After cooled down to room temperature, the synthetic products were ground for subsequent analysis.

**Characterization.** The samples were characterized by powder X-ray diffraction (XRD) performed on a Panalytical X'Pert diffractometer using  $\text{Cu K}\alpha$  radiation ( $\lambda=0.154187\text{ nm}$ ). All of the patterns within the  $10\text{-}90^\circ$   $2\theta$  range were collected in a scanning mode with a step size of  $0.02^\circ$ . The morphology patterns of samples were obtained on a field emission scanning electron microscope (SEM JSM-6700F) equipped with an Energy Dispersive Spectrometer spectra (EDS) and transmission electron microscope (TEM JEOL-2010).

#### ***In situ* Temperature-dependent synchrotron X-ray diffraction**

The powders were loaded into 1.0 mm diameter corundum capillaries. The capillary was then mounted on the thermal stage of beamline 14B1, at Shanghai Synchrotron Radiation Facility (SSRF). The wavelength used at the 14B1 was  $0.6887\text{ \AA}$  (18 KeV). The detailed information about beamline BL14B1 can be found in our previous work<sup>48</sup>. To track the structural changes accompanied with the temperature changes, SXRD spectra continuously were recorded as a set of circles on a two-dimensional

image plate detector in the transmission mode during heating from room temperature to 400 °C (i.e., heating rate = 5 °C min<sup>-1</sup>). The total recording time for one spectrum was approximately 30 s.

### ***In situ* Temperature-dependent Raman spectroscopy**

*In situ* Raman spectroscopy was carried out using Renishaw inVia Reflex Raman microscope. Sample powders pressed into sheet were fixed in the heating device with N<sub>2</sub> as protective atmosphere. The laser with wavelength 532 nm was selected as the illuminant with around 1 μm diameter. The power of the laser was set below 1 mW/μm<sup>2</sup> to avoid sample damage. The acquisition time of each Raman spectrum was 12 s to 5 times for every 25 °C from room temperature to 500 °C. The laser spot was constantly adjusted through the microscope to make the beam stay at the same place during heating. The collected Raman spectra were fitted using Gauss and Voigt functions.

### ***In situ* Temperature-dependent photoluminescence**

The temperature-dependent UC (DS) luminescence spectra were evaluated by a FLS980 spectrophotometer equipped with a CW 980nm diode laser (LASEVER INC. LSR980CP-FC-9W) as excitation source, and R928P (NIR-PMT) photomultiplier as detector as well as a temperature control instrument (Linkam THMS600). The temperature-dependent luminescence decay curves were measured by a FLS980 instrument equipped with 980 nm pulse laser diode (laser: LASEVER INC. LSR980CP-FC-9W; signal generator: JDS6600). UC photographs at various temperatures were taken by the visible Nikon D750 camera under CW 980nm laser (laser power: 0.57 W/cm<sup>3</sup>). To avoid interference of 980 nm laser, the GRB3 filter was added in the front of the visible camera. Photographs NIR downshifting of Sc<sub>2</sub>(MoO<sub>4</sub>)<sub>3</sub>:Yb/Er at various temperatures were taken by a NIR camera (Photonic Science). To avoid interference of 980 nm laser (laser power: 0.32 W/cm<sup>3</sup>), the 1250 nm long-pass filter was added in the front of a NIR camera.

## **References**

1. Pust P. *et al.*, Narrow-band red-emitting Sr[LiAl<sub>3</sub>N<sub>4</sub>]:Eu<sup>2+</sup> as a next-generation LED-phosphor material. *Nat. Mater.*, **13**, 891-896 (2014).

2. Liu M. M. *et al.*, Suppression of temperature quenching in perovskite nanocrystals for efficient and thermally stable light-emitting diodes. *Nat. Photonics*, **15**, 379-385 (2021).
3. Wei Y. *et al.*, Strategies for designing antithermal-quenching red phosphors. *Adv. Sci.*, **7**, 1903060-1903068 (2020).
4. Huo J. S. *et al.*, Efficient energy transfer from trap levels to  $\text{Eu}^{3+}$  leads to antithermal quenching effect in high-power white light-emitting diodes. *Inorg. Chem.*, **59**, 15514–15525 (2020).
5. Kim Y. H. *et al.*, A zero-thermal-quenching phosphor. *Nat. Mater.*, **16**, 543-550 (2017).
6. Liu S. Y. *et al.*, Wide range zero-thermal-quenching ultralong phosphorescence from zero-dimensional metal halide hybrids. *Nat. Commun.*, **11**, 1-9 (2020).
7. Cui X. S. *et al.*, Size-dependent abnormal thermo-enhanced luminescence of ytterbium doped nanoparticles. *Nanoscale*, **9**, 13794-13799 (2017).
8. Shi R. *et al.*, Thermal enhancement of upconversion emission in nanocrystals: a comprehensive summary. *Phys. Chem. Chem. Phys.*, **23**, 20-42 (2021).
9. Zou H. *et al.*, Thermal enhancement of upconversion by negative lattice expansion in orthorhombic  $\text{Yb}_2\text{W}_3\text{O}_{12}$ . *Angew. Chem. Int. Ed.*, **58**, 17255-17259 (2019).
10. Zou H. *et al.*, Simultaneous enhancement and modulation of upconversion by thermal stimulation in  $\text{Sc}_2\text{Mo}_3\text{O}_{12}$  crystals, *J. Phys. Chem. Lett.*, **11**, 3020-3024 (2020).
11. Dang P. *et al.*, Thermally stable and highly efficient red-emitting  $\text{Eu}^{3+}$ -doped  $\text{Cs}_3\text{GdGe}_3\text{O}_9$  phosphors for WLEDs: non-concentration quenching and negative thermal expansion, *Light Sci. Appl.*, **10**, 29-41 (2021).
12. Wu D. *et al.*, Negative thermal quenching of photoluminescence in a copperorganic framework emitter, *Chem. Comm.*, **56**, 12057-12060 (2020).
13. Lei L. *et al.*, Enhancing negative thermal quenching effect via low-valence doping in two-dimensional confined core-shell upconversion nanocrystals, *J. Mater. Chem. C.*, **6**, 11587-11592 (2018).
14. Ren B. *et al.*, Synthesis of core-shell  $\text{ScF}_3$  nanoparticles for thermal enhancement of upconversion, *Chem. Mater.*, **33**, 158-163 (2020).
15. Wu Y. *et al.*, Negative thermal quenching of photoluminescence in annealed  $\text{ZnO-Al}_2\text{O}_3$  core-shell nanorods. *Phys. Chem. Chem. Phys.*, **17**, 5360-5365 (2015)
16. Huang X. *et al.*, Green luminescence from Cu-doped ZnO nanorods: Role of Zn vacancies and negative thermal quenching. *Appl. Phys. Lett.*, **102**, 111106 (2013)
17. He H. *et al.*, Negative thermal quenching behavior and Long luminescence lifetime of surface-state related green emission in ZnO nanorods. *J. Phys. Chem. C.*, **112**, 14262-14265 (2008).
18. Wang J. *et al.*, Enhancing multiphoton upconversion through energy clustering at sublattice level. *Nat. Mater.*, **13**, 157–162 (2014).
19. Yamamura Y. *et al.*, Characteristic phonon spectrum of negative thermal expansion materials with framework structure through calorimetric study of  $\text{Sc}_2\text{M}_3\text{O}_{12}$  (M = W and Mo), *Chem. Mater.*, **21**, 3008-3016 (2009).
20. Sumithra S. *et al.*, Negative thermal expansion in rare earth molybdates. *Solid State Sci.*, **8**, 1453-1458 (2006).
21. Evans J. S.O. *et al.*, Structural phase transitions and negative thermal expansion in  $\text{Sc}_2(\text{MoO}_4)_3$ . *Inter. J. Inorg. Mater.*, **2**, 143-151 (2000).

22. Blasse G., Energy transfer in oxidic phosphors. *Philips Res. Rep.*, **24**, 131-136 (1969).
23. Liu X. F. *et al.*, Recent advances in energy transfer in bulk and nanoscale luminescent materials: from spectroscopy to applications. *Chem. Soc. Rev.*, **44**, 8714-8746 (2015).
24. Dong H. *et al.*, Energy transfer in lanthanide upconversion studies for extended optical applications. *Chem. Soc. Rev.*, **44**, 1608-1634 (2015).
25. Gong X. W. *et al.*, Electron-phonon interaction in efficient perovskite blue emitters. *Nat. Mater.*, **17**, 550-556 (2018).
26. Ding S. Y. *et al.*, Nanostructure-based plasmon-enhanced Raman spectroscopy for surface analysis of materials. *Nat. Rev. Mater.*, **1**, 16021 (2016).
27. Paraguassu W. *et al.* A comparative study of negative thermal expansion materials  $\text{Sc}_2(\text{MoO}_4)_3$  and  $\text{Al}_2(\text{WO}_4)_3$  crystals. *Vib. Spectrosc.*, **44**, 69-77 (2007).
28. Yuan L. *et al.*, Syntheses of negative thermal expansion materials  $\text{Sc}_2(\text{MO}_4)_3$  (M = W, Mo) with a  $\text{CO}_2$  laser and their Raman spectra. *Acta Phys. Sin.*, **63**, 248106-248115 (2014).
29. Guy S., Modelization of lifetime measurement in the presence of radiation trapping in solid-state materials. *Phys. Rev. B* **73**, 144101-8 (2006).
30. Sumida D. S. *et al.*, Effect of radiation trapping on fluorescence lifetime and emission cross section measurement in solid-state laser media. *Opt. Lett.*, **19**, 1343-1345 (1994).
31. Wang F. *et al.* Tuning upconversion through energy migration in core-shell nanoparticles. *Nat. Mater.*, **10**, 968-973 (2011).
32. Shang M. M. *et al.*, How to produce white light in a single-phase host? *Chem, Soc. Rev.*, **43**, 1372-1386 (2014).
33. Li A. M. *et al.*, A novel anion doping strategy to enhance upconversion luminescence in  $\text{NaGd}(\text{MoO}_4)_2:\text{Yb}^{3+}/\text{Er}^{3+}$  nanophosphors. *Phys. Chem. Chem. Phys.*, **19**, 15693-15700 (2017).
34. Dramianin M. D. Sensing temperature via downshifting emissions of lanthanide-doped metal oxides and salts. A review. *Methods Appl. Fluoresc.*, **4**, 042001 (2016).
35. Jaque D. *et al.* Luminescence nanothermometry. *Nanoscale* **4**, 4301-4326 (2012).
36. McLaurin E. J. *et al.*, Dualemitting nanoscale temperature sensors. *Chem. Mater.* **25**, 1283-1292 (2013).
37. Y. Gao, F. Huang, H. Lin, J. C. Zhou, J. Xu and Y. S. Wang, A novel optical thermometry strategy based on diverse thermal response from two intervalence charge transfer states. *Adv. Funct. Mater.* **26**, 3139-3145 (2016).
38. Ji Z. L. *et al.*, Heating-induced abnormal increase in  $\text{Yb}^{3+}$  excited state lifetime and its potential application in lifetime luminescence nonothermometry. *Inorg. Chem. Front.*, **6**, 110-116 (2019).
39. Wu M. *et al.*, A spatial/temporal dual-mode optical thermometry based on double-sites dependent luminescence of  $\text{Li}_4\text{SrCa}(\text{SiO}_4)_2:\text{Eu}^{2+}$  phosphors with highly sensitive luminescent thermometer. *Chem. Eng. J.*, **396**, 125178 (2020).
40. Savchuk O. A. *et al.*, Er: Yb:  $\text{NaY}_2\text{F}_5\text{O}$  up-converting nanoparticles for sub-tissue fluorescence lifetime thermal sensing. *Nanoscale*, **6**, 9727-9733 (2014)
41. Trejgis K. *et al.*, The influence of manganese concentration on the sensitivity of bandshape and lifetime luminescent thermometers based on  $\text{Y}_3\text{Al}_5\text{O}_{12}:\text{Mn}^{3+}$ ,  $\text{Mn}^{4+}$ ,  $\text{Nd}^{3+}$  nanocrystals. *Phys. Chem. Chem. Phys.*, **20**, 9574-9581 (2018).
42. Chen Y. B. *et al.*, Dual-mode optical thermometry design in  $\text{Lu}_3\text{Al}_5\text{O}_{12}:\text{Ce}^{3+}/\text{Mn}^{4+}$  phosphor. *Inorg. Chem.*, **59**, 1383-1392 (2020).

43. Zhang H. *et al.*, Highly sensitive dual-mode optical thermometry in double perovskite oxides via Pr<sup>3+</sup>/Dy<sup>3+</sup> energy transfer. *Inorg. Chem.*, **59**, 14337-14346 (2020).
44. Gao Y. *et al.*, Broadening the valid temperature range of optical thermometry through dual-mode design. *J. Mater. Chem. C* **6**, 7462-7478 (2018).
45. Xiang, G. *et al.* Dual-mode optical thermometry based on the fluorescence intensity ratio excited by a 915 nm wavelength in LuVO<sub>4</sub>:Yb<sup>3+</sup>/Er<sup>3+</sup>@SiO<sub>2</sub> nanoparticles. *Inorg. Chem.*, **58**, 8245-8252 (2019).
46. Ximendes, E. C. *et al.* In vivo subcutaneous thermal video recording by supersensitive infrared nanothermometers, *Adv. Funct. Mater.*, **27**, 1702249 (2017).
47. Liu X. *et al.*, Interaction of crystal water with the building block in Y<sub>2</sub>Mo<sub>3</sub>O<sub>12</sub> and the effect of Ce<sup>3+</sup> doping. *Phys. Chem. Chem. Phys.*, **16**, 12848-12857 (2014).
48. Yang T. *et al.*, Introduction of the X-ray diffraction beamline of SSRF. *Nucl. Sci. Tech.*, **26**, 020101(2015).

## Acknowledgements

This work was financially supported by the National Natural Science Foundation of China (No. 51862012, U1805252) and Jiangxi Provincial Natural Science Foundation (No. 20202BAB204008) as well as the Innovation Leadership Program of Ganzhou, and the CAS/SAFEA International Partnership Program for Creative Research Teams. The authors thank beamline BL14B1 (Shanghai Synchrotron Radiation Facility) for providing the beam time and assistance.

## Data availability.

The data that support the findings of this study are available from the corresponding authors on request.

## Author contributions

J. L. conceived the idea and designed the research. M. H. and Z. H. synthesized and characterized materials. F. L. performed temperature-dependent luminescence spectra. J. L., D. T., X. Y. and B. Q. analyzed the data and wrote the paper. H. W. supervised all the research. All the authors contributed to the discussion and provided feedback on the manuscript.

## Additional information

Supplementary Information accompanies this paper at

<http://www.nature.com/naturecommunications>

## **Competing financial interests**

The authors declare no competing financial interests.

## Supplementary Files

This is a list of supplementary files associated with this preprint. Click to download.

- [SupplementaryInfor.docx](#)